coatings

MDPI

Article

Impurity Phases and Optoelectronic Properties of $CuSbSe_2$ Thin Films Prepared by Cosputtering Process for Absorber Layer in Solar Cells

Sara Kim and Nam-Hoon Kim *

Department of Electrical Engineering, Chosun University, Gwangju 61452, Korea; zomidi@gmail.com
* Correspondence: nhkim@chosun.ac.kr; Tel./Fax: +82-62-230-7028

Received: 23 November 2020; Accepted: 8 December 2020; Published: 11 December 2020

Abstract: When there is a choice of materials for an application, particular emphasis should be given to the development of those that are low-cost, nontoxic, and Earth-abundant. Chalcostibite $CuSbSe_2$ has gained attention as a potential absorber material for thin-film solar cells, since it exhibits a high absorption coefficient. In this study, $CuSbSe_2$ thin films were deposited by radio frequency magnetron cosputtering with $CuSe_2$ and Sb targets. A series of $CuSb_xSe_2$ thin films were prepared with different Sb contents adjusted by sputtering power, followed by rapid thermal annealing. Impurity phases and surface morphology of Cu–Sb–Se systems were directly affected by the Sb sputtering power, with the formation of volatile components. The crystallinity of the $CuSbSe_2$ thin films was also enhanced in the near-stoichiometric system at an Sb sputtering power of 15 W, and considerable degradation in crystallinity occurred with a slight increase over 19 W. Resistivity, carrier mobility, and carrier concentration of the near-stoichiometric thin film were 14.4 Ω-cm, 3.27 $cm^2/V \cdot s$, and 1.33×10^{17} cm^{-3}, respectively. The optical band gap and absorption coefficient under the same conditions were 1.7 eV and 1.75×10^5 cm^{-1}, which are acceptable for highly efficient thin-film solar cells.

Keywords: $CuSbSe_2$ thin film; cosputtering; optical and electrical properties

1. Introduction

Considerable attention has recently been given to thin-film solar cells based on high-efficiency absorbers owing to their applicability in flexible photovoltaic technology. $CuInGaSe_2$ thin-film solar cells have already achieved a conversion efficiency of 23.4% [1]; however, the scarcity of In and high cost of Ga have restricted their mass production. Alternative CdTe thin-film absorber was progressed to the commercialization stage, but was stranded by toxicity and environmental pollution of Cd. Cu_2-II-IV-VI_4 (II = Zn; IV = Si, Ge, Sn; VI = S, Se, Te) quaternary compounds, represented by Cu_2ZnSnS_4 or $Cu_2ZnSnSe_4$, were proposed as an effort to replace the above deficient and expensive elements [2,3]. Up to 12.6% (theoretically 18.47%) of energy conversion efficiency was achieved, but difficulties in the control of composition and morphology still remain in the quaternary compound [4,5]. Hence, thin-film solar cells with Earth-abundant and nontoxic materials need to be investigated as possible candidates. Toward this goal, different compounds of Cu–Sb–Se and Cu–Sb–S are being considered as potential low-cost sustainable absorber materials for inorganic thin-film solar cells. Copper antimony selenide ($CuSbSe_2$) is a p-type semiconductor, which is due to an excess of volatile components (e.g., Sb and a chalcogen) to cause the formation of copper vacancy acceptors [6]. $CuSbSe_2$ with an orthorhombic crystalline structure and Pnma space group (No. 62) [7,8] is an important chalcogenide semiconductor owing to its narrow direct band gap (~1.1 eV) [9] and high absorption coefficient (>10^4 cm^{-1}) [9,10], which favors its application in optoelectronics and photovoltaics [11]. Trivalent Sb (Sb^{3+}) with lone-pair $5s^2$ electrons is known to be responsible for the large absorption coefficient of $CuSbSe_2$ [12]. It was found that the Cu–Sb–Se system is complicated, containing numerous reported phases with low crystallographic symmetry compared with chalcopyrite materials [6,10,13–15]. In the Cu–Sb–Se system, besides $CuSbSe_2$, there are at least five binary or ternary phases including Cu_2Se, CuSe, Sb_2Se_3, Cu_3SbSe_4, and Cu_3SbSe_3 that could exist as secondary phases if the samples are nonstoichiometric or prepared with an inappropriate process [16,17]. Even minor deviations from the $CuSbSe_2$ stoichiometry lead to the precipitation of impurity phases. The window in Cu:Sb:Se ratio for creating $CuSbSe_2$ seems to be narrow and needs to be close to 1:1:2 to prevent the formation of these secondary phases. Some of these phases are highly conductive and can cause a shunting effect [18], while some of these phases such as Sb_2Se_3 have excellent optoelectronic properties [11], so strict phase control is important for the prevention of these destructive effects. The importance of rigorous control of the Cu content in thin films for the prevention of phases such as Cu_2Se and Cu_3SbSe_3 has been emphasized in many previous reports [5,6,12], when the Sb content is another important factor for the prevention of these secondary phases. Several methods, such as electrodeposition, pulsed laser deposition, sequential evaporation with selenization, spin-coating, and pre-sputtering of Cu with close-spaced sublimation of Sb_2Se_3, have been reported to prepare $CuSbSe_2$ thin films [19]. The magnetron sputtering method offers some merits of superior adhesion of thin films, excellent transfer of composition, uniform surface morphology, straightforward control of deposition rate, low-cost equipment, and possibility for large-area deposition in the full-vacuum operation [20]. The cosputtering method can also provide a simultaneous one-step process with controllable composition of the thin films without involving the highly toxic and explosive chemical nature of the post-selenization process in the use of expensive equipment. Only a few studies have reported on the fabrication and characterization of $CuSbSe_2$ thin films using the cosputtering method with Cu_2Se/Sb_2Se_3 and Cu/Sb_2Se_3 target combinations [9,21,22]. The focus of this study was on the phases and the evolution of orientation of $CuSbSe_2$ thin films deposited using a radio frequency (RF) magnetron cosputtering system directly with $CuSe_2$ and Sb targets, while $CuSe_2$ generally has a cubic and orthorhombic structure that incongruently melts at 347 °C, forming CuSe and a Se-rich liquid [23]. A series of $CuSb_xSe_2$ thin films were prepared with various levels of Sb content at the same thickness, adjusted by sputtering power for Sb and deposition time. Then, all samples were annealed in a rapid thermal annealing (RTA) system to prevent the volatility of Se. Phase and crystal orientation evolution with changing Sb content were investigated for the absorber materials in thin-film solar cells.

2. Experimental Details

$CuSbSe_2$ thin films were deposited on $1 \times 1\ cm^2$ Corning glass substrates using an RF magnetron cosputtering system (IDT Engineering Co., Gyeonggi, Korea) [24–27], as shown in Figure S1, with $CuSe_2$ (TASCO, Seoul, Korea, 99.99% purity, 2-inch diameter) target under a fixed power of 40 W and variable power for Sb (TASCO, 99.99% purity, 2-inch diameter) target from 13 to 21 W in increments of 2 W, while other parameters were kept constant using the following conditions: presputtering process for 5 min prior to each run, an Ar gas flux of 20 sccm, base pressure of 1.0×10^{-6} Torr, substrate-to-target distance of 5.0 cm, and vacuum pressure of 7.5×10^{-3} Torr during sputtering at room temperature. During the target cleaning procedure, the substrates were shielded with a shutter. The deposition time was adjusted from 34 to 28 min in order to obtain a constant thickness of approximately 450 nm for the proper comparison of crystallographic properties. After sputtering deposition, the samples were subjected to an RTA (GRT-100, GD-Tech Co., Gyeongsangbuk, Korea) process at 350 °C for 30 min under a N_2 gas atmosphere. The crystalline structure of the thin films was analyzed using X-ray diffraction (XRD, PANalytical B.V., Almelo, The Netherlands, X'pert-PRO-MRD, Cu Kα = 0.15405 nm, 40 kV, 30 mA). A field emission scanning electron microscope (FESEM, Hitachi, Tokyo, Japan, S-4700, without Pt coating) was employed to reveal the morphological characteristics of the Cu–Sb–Se thin films. An energy dispersive X-ray spectrometer (EDS) attached to the FESEM and X-ray photoelectron spectroscopy (XPS, Thermo Fisher Scientific Inc., Waltham, MA, USA, K-Alpha$^+$) were used to analyze the compositional analysis and chemical nature of the Cu–Sb–Se thin films. The optical properties of the

Cu–Sb–Se thin films were measured using a UV-visible spectrophotometer (Varian Techtron, Mulgrave, Australia, Cary500scan) in the range 200–3000 nm. The electrical properties, including the carrier concentration, resistivity, and mobility of the Cu–Sb–Se thin films were characterized using a Hall effect measurement system (Accent Optical Technologies, Bend, OR, USA, HL5500PC) at room temperature.

3. Results and Discussion

The surface morphology of Cu–Sb–Se thin films deposited at different Sb powers was analyzed using FESEM. Figure 1 shows cross-sectional and surface FESEM images of the Cu–Sb–Se thin films annealed at 350 °C for 30 min. All as-deposited thin films showed a smooth and dense surface morphology (Figure S2). For the annealed thin films, the surface morphology changed with the sputtering power for Sb. Annealed Cu–Sb–Se thin films with a sputtering power for Sb of 13 W showed smooth and dense surface morphology like the as-deposited thin films. Annealed thin films with 15 W of power showed a smooth surface morphology with clear grain boundaries. A gap on the surface appeared in the annealed thin films at 15 W which was not seen in the as-deposited thin films under the same sputtering power. As shown in Figure 1d,e, with an increase in the sputtering power for Sb to 19 and 21 W, the surface showed more pores and larger gaps between particles. Although the Sb content increased at Sb powers of 19 and 21 W and the annealing process was performed at a much lower temperature than the melting point of $CuSbSe_2$ (480 °C), the $CuSbSe_2$ could decompose to gaseous Sb_2Se_3 which could leave gaps and escape from the surface of the thin films [10,19]. The resulting porous and nonuniform surface with the large gaps appears to be unsuitable for the absorption layer in solar cells.

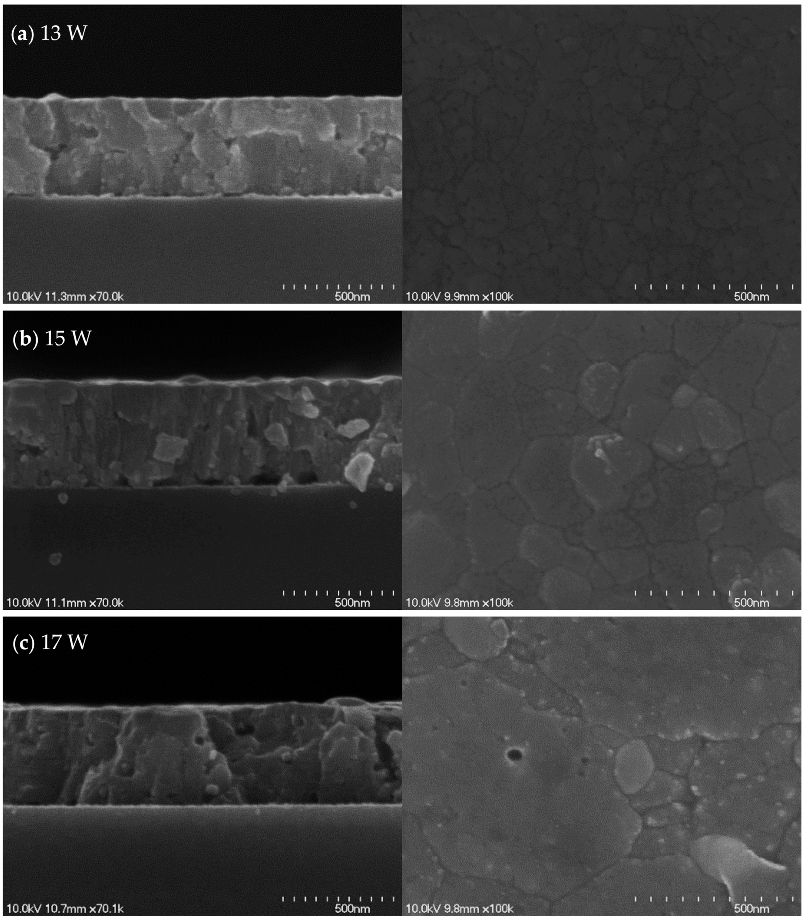

Figure 1. *Cont.*

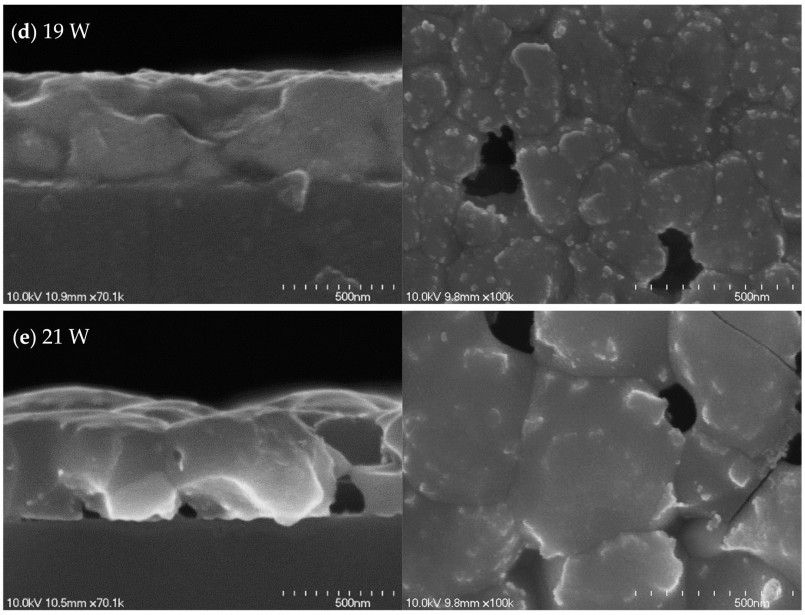

Figure 1. Cross-sectional and surface field emission scanning electron microscope (FESEM) images of annealed thin films with different sputtering powers for Sb: (**a**) 13, (**b**) 15, (**c**) 17, (**d**) 19, and (**e**) 21 W.

Elemental analysis of the as-deposited and annealed Cu–Sb–Se thin films was carried out through EDS measurements. Figure 2 shows the changes in elemental composition for the as-deposited and annealed thin films, including the atomic percentage for each element as well as the atomic ratio in the thin films. The EDS results for the as-deposited thin film with 13 W show a Cu-rich and Sb-poor composition compared to the ideal stoichiometric ratio, whereas that with 15 W is the closest to the stoichiometric ratio of 1:1:2 among the as-deposited thin films. All the as-deposited thin films exhibit Cu-rich and Se-poor conditions. The atomic percentage of Sb in the as-deposited thin films increase from 8.91% to 21.22% with an increase in the sputtering power for Sb, as shown in Figure 2a. Meanwhile, the atomic percentages of Sb and Se start to decrease together in the annealed thin films above an Sb sputtering power of 17 W, which is attributed to the decomposition of $CuSbSe_2$ into Sb_2Se_3 and/or sublimation of Sb_2Se_3 into the gaseous state [14,18]. As shown in Figure 1d,e of the FESEM images, the annealed thin films at 19 and 21 W show large gaps on the surface, in good agreement with the EDS results. At higher Sb sputtering powers, the higher atomic percentages of Sb lead to an increase in the probability of forming volatile Sb_2Se_3 (g) with high vapor pressure, and a higher amount of volatile Sb_2Se_3, leading to more and/or larger gaps on the surface. $CuSbSe_2$ is still stable but starts to decompose at the sputtering powers of 19 and 21 W, corresponding to Cu-rich, Sb-rich, and Se-poor conditions in the as-deposited thin film, while the phases in the thin films may strongly depend on the growth conditions [10,28]. These gaps seem to lead to the degradation of the optical quality of the thin films, so those conditions are not appropriate for the absorption layer in solar cells [19].

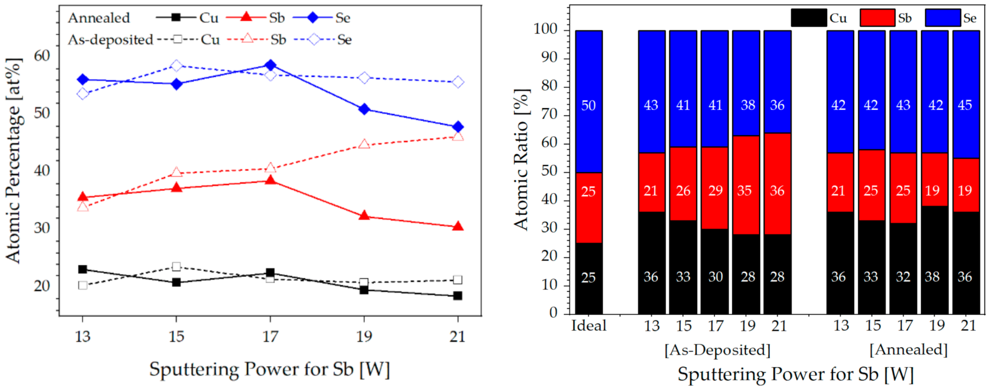

(**a**) (**b**)

Figure 2. (**a**) Atomic percentage and (**b**) atomic ratio for each element of the as-deposited and annealed thin films with different sputtering powers for Sb of 13, 15, 17, 19, and 21 W.

All as-deposited Cu–Sb–Se thin films exhibited an amorphous nature (not shown). An RTA treatment was carried out for the purpose of improving the crystallinity of the Cu–Sb–Se thin films. Figure 3 shows the XRD patterns of the annealed Cu–Sb–Se thin films at various Sb sputtering powers. The XRD patterns of the annealed thin film at 13 W show Cu_3SbSe_3 as the dominant peak along the (122) plane at $2\theta = 33.2°$, while secondary phases corresponding to Cu_2Se also appear with less intensity along the (102), (111), (103), and (211) planes at $2\theta = 26.2°, 30.5°, 31.2°$, and $45.5°$, respectively. Only two intermetallic compounds, Cu_3SbSe_3 and Cu_2Se, were observed under these conditions. These are the typical intermediate phases during the formation of $CuSbSe_2$ [19] in Cu-rich composition [18], and EDS analysis revealed a Cu:Sb:Se ratio of 36:21:43 in the as-deposited thin film, as shown in Figure 2b. The Cu_3SbSe_3 impurity phase is known as a p-type semiconductor with a low resistivity, a carrier density in the order of 10^{18} cm^{-3}, and a band gap within the range 1.25–1.50 eV [29–31]. The XRD pattern of the annealed thin film at 15 W shows two dominant phases: Sb_2Se_3 and $CuSbSe_2$. The formation of the Sb_2Se_3 phase is confirmed by the presence of a dominant peak (004) along the preferred orientation at $2\theta = 23.7°$. The $CuSbSe_2$ phase shows peaks along the (002), (112), and (304) planes centered at $2\theta = 11.8°, 28.6°$, and $48.8°$, respectively. XRD peaks indicating the presence of other phases, such as Cu_3SbSe_3 and Cu_2Se in the thin film have relatively low intensity. Diffraction peaks along (111) and (103) planes at 30.5° and 31.2° corresponded to the Cu_2Se. Diffraction peaks at 33.2° and 33.8° are indexed to the (122) and (040) planes corresponding to Cu_3SbSe_3. As confirmed from the EDS results (Figure 2), although this condition has the ratio closest to the stoichiometric ratio of 1:1:2, it still shows a Cu-rich and Sb-rich composition. Sb-rich composition causes an increase in the amount of Sb_2Se_3 [10]. Sb_2Se_3 is a p-type semiconductor that exhibits low electrical conductivity with an excellent photoresponse [32–34], and crystallizes in a one-dimensional structure where the ribbons are held together by van der Waals forces [35]. This structure contributes to poor carrier transport and mobility between the ribbons [36] with various reported band gaps in the range of 1.2–1.8 eV [37,38]. The XRD pattern of the annealed thin film with 17 W of sputtering power does not show any dominant peak, but there are many peaks with low intensity, as shown in Figure 3c. As the atomic ratio of Sb increases, more Sb_2Se_3 is formed and some of it sublimates on the surface, which is why the intensity of the peak corresponding to Sb_2Se_3 in this condition is less than that using 15 W. The XRD patterns of the annealed thin films at 19 and 21 W of sputtering powers are almost identical, with the atomic ratio of Sb close to that of Se, and extra Sb leading to the formation of a large amount of Sb_2Se_3 in the gaseous phase owing to its high vapor pressure [16]. Sb_2Se_3 sublimates and leaves the thin films to form a porous surface, as shown in Figure 1d,e, which explains the lower intensity of the (004) preferred orientation under these conditions. Several small diffraction peaks are observed at $2\theta = 23.7°$, 27.3°, and 28.6° along the (004), (130), and (112) preferred orientations corresponding to Sb_2Se_3, Sb_2O_3, and $CuSbSe_2$, respectively. Other peaks centered at 30.5° and 31.2° are indexed to the (111) and (103) planes corresponding to Cu_2Se. Peaks along the (122) and (040) planes are observed at 33.2° and 33.8°, corresponding to the Cu_3SbSe_3. In Sb-rich conditions, some elemental Sb remains intact on the surface or reacts with oxygen to form Sb_2O_3 [14]. Another peak appears at $2\theta = 36.4°$ along the (111) orientation corresponding to Cu_2O. Slight oxidation of the surface was frequently observed for thin films prepared at sputtering power for Sb of 17, 19, and 21 W.

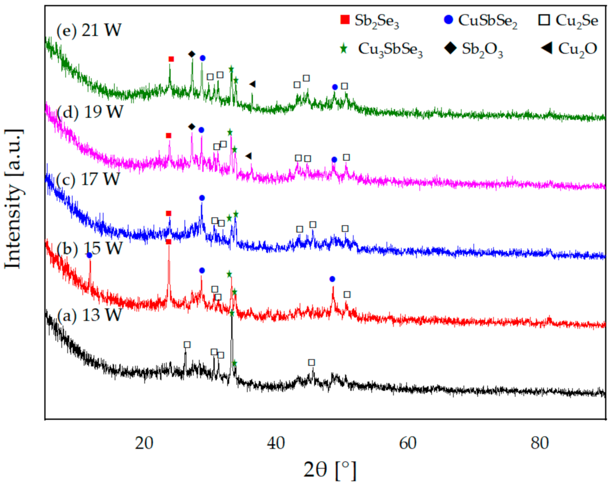

Figure 3. X-ray diffraction patterns of annealed Cu-Sb-Se thin films with different sputtering powers for Sb: (**a**) 13, (**b**) 15, (**c**) 17, (**d**) 19, and (**e**) 21 W.

The valence states of each element were evaluated using XPS in the annealed $CuSbSe_2$ thin films at sputtering powers for Sb of 15 and 21 W, which showed the sharp difference in XRD analysis of Figure 3. All XPS spectra were deconvoluted using XPSPEAK4.1 software. The spectrum of the C 1*s* peak with a binding energy of 285 eV was used as a reference for data calibration. High-resolution narrow scans were employed to examine the core level elements, such as Cu 2*p*, Sb 3*d*, and Se 3*d*, corresponding to Cu^+, Sb^{3+}, and Se^{2-} oxidation states, respectively, in Cu–Sb–Se composites. The oxidation state of Cu is presented in Figure 4a,b. For both 15 and 21 W, the Cu 2*p* doublet is symmetric and narrow at a binding energy of 932.18 eV (Cu $2p_{3/2}$) and 952.00 eV (Cu $2p_{1/2}$) with spin-orbit splitting (SOS) energy of 19.82 eV corresponding to Cu^+ in the thin films reported for Cu_2Se, $CuSbSe_2$, Cu_3SbSe_3, and Cu_2O [38–41]. According to Coster–Kronig broadening effects [42], the full width at half maximum (FWHM) of the Cu $2p_{3/2}$ peak is slightly narrower than that of the Cu $2p_{1/2}$ peak. It is well known that Cu^+ in Cu_2Se, $CuSbSe_2$, and Cu_3SbSe_3 can be oxidized to Cu^{2+} in CuO [38]; however, no peak related to Cu^{2+} is observed in either Figure 4a or Figure 4b. For Sb, a doublet of the Sb 3*d* peak is observed, while the peaks around 35–37 eV related to Sb 4*d* correspond to Sb^{5+}. For the annealed thin films with 15 and 21 W, intense double peaks for Sb $3d_{5/2}$ and Sb $3d_{3/2}$ are observed at the lower binding energy pair of 528.9 and 538.3 eV and the higher binding energy pair of 530.2 and 539.6 eV with an SOS energy of 9.3 eV corresponding to Sb^{3+} reported for $CuSbSe_2$, Sb_2Se_3, and Cu_3SbSe_3 [38,40,41]. The $3d_{5/2}$ peaks at 528.1 eV and $3d_{3/2}$ at 537.4 eV are consistent with pure Sb, which was observed in the thin film with 15 W, indicating that some elemental Sb remains intact on the surface of the thin film. For the annealed thin films at 21 W, an O 1*s* peak overlapping with the Sb 3*d* peak, corresponding to the O^{2-} oxidation state, is observed in the XPS result related to Sb_2O_3, confirming slight oxidation on the surface, as shown in Figure 4d. The Se 3*d* peak, showing an Se $3d_{5/2}$ peak at 53.8 eV and an Se $3d_{3/2}$ peak at 54.7 eV with an SOS energy of 0.9 eV, confirms the presence of the Se^{2-} oxidation state in both the annealed thin films at 15 and 21 W reported for Cu_2Se, $CuSbSe_2$, Cu_3SbSe_3, and Sb_2Se_3 [40–42].

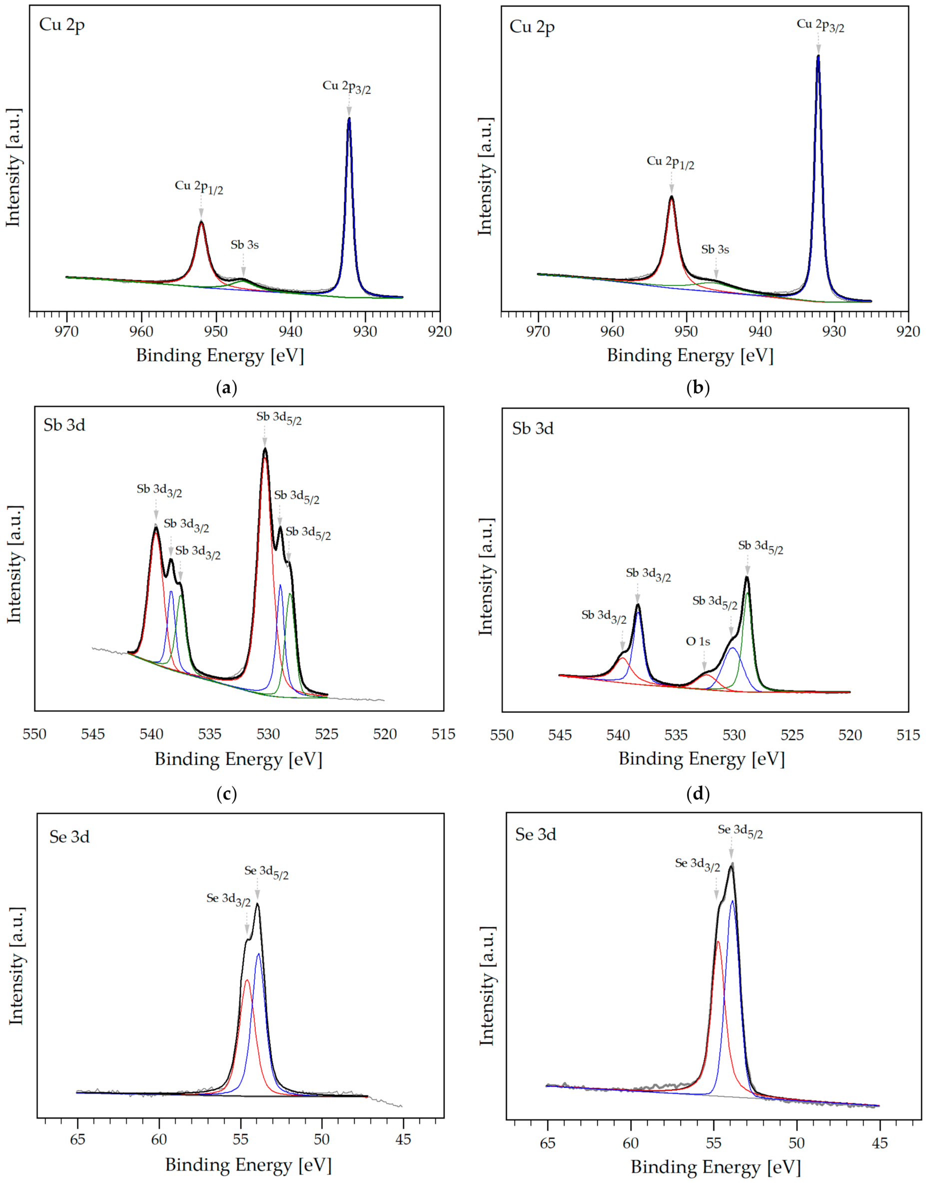

(a) (b) (c) (d) (e) (f)

Figure 4. X-ray photoelectron spectra of (**a**,**b**) Cu 2*p*, (**c**,**d**) Sb 3*d*, and (**e**,**f**) Se 3*d* obtained from annealed $CuSbSe_2$ thin films with sputtering powers for Sb of (**a**,**c**,**e**) 15 and (**b**,**d**,**f**) 21 W.

The electrical properties, including resistivity (ρ), carrier mobility (μ), and carrier concentration (n), of the annealed $CuSbSe_2$ thin films were analyzed using Hall effect measurements (Table S1). Electrical conductivity is generally sensitive to multiscale defect scattering carriers, such as point defects, dislocations, pores, and grain boundaries in thin films [43]; point defects can be formed by the growth conditions and can directly affect the electrical conductivity of the thin films. Possible point defects include acceptor-like Cu vacancies (V_{Cu}) and Cu–Sb antisites (Cu_{Sb}) as well as donor-like Se vacancies (V_{Se}), Sb-Cu antisites (Sb_{Cu}), and Cu interstitials (Cu_i) in the $CuSbSe_2$ thin films. Among them, the most probable point defect in the $CuSbSe_2$ thin films is V_{Cu}, owing to shallow V_{Cu} defects with the lowest formation energy [44], and it has the greatest influence on the electrical conductivity. All the annealed thin films in this study exhibit p-type conductivity, which should be determined mainly by V_{Cu} acceptors. With an increase in the sputtering power for Sb, there are more deviations (Figure 2b) from the stoichiometric composition, leading to the formation of intrinsic point defects in the compound [3]. Figure 5 shows that the carrier concentrations are in the order of 10^{17} cm^{-3} in all the annealed thin films in accordance with previous reports [9,10,45], except for 17 W of sputtering power, which is in the order of 10^{16} cm^{-3}. The carrier concentration also slightly increased with an increase in the sputtering power for Sb, while a higher carrier concentration at higher Sb sputtering power is inferred from the higher point defect density [46]. Under Se-poor, Cu-rich, and Sb-rich conditions, which were observed in the as-deposited thin films with Sb powers of 15, 17, 19, and 21 W, the V_{Cu} acceptors and Cu_i donors are the most easily formed defects and are thus considered to be the dominant defects, leading to high carrier concentration as Sb power increases [14]. On the other hand, the population of other point defects has much higher formation energies for contribution to the carrier concentration than the dominant defects. An excess of Sb with an increase in the Sb sputtering power increases the population of V_{Cu}, and thus causes the carrier concentration to show an upward tendency. The carrier mobility is in the range 1.89–5.77 $cm^2/V{\cdot}s$, as shown in Figure 5, which is less than previously reported values for $CuSbSe_2$ due to the impurity phases of Sb_2Se_3 and Cu_2Se with lower mobility values than $CuSbSe_2$ in thin films [45,47]. The carrier mobility at 21 W of sputtering power shows a sudden decrease correlated not only to large gaps interfering with carriers to move from grain to neighboring grain but also to the slight surface oxidation producing a potential barrier [48,49], as shown in Figures 1e and 3. As shown in Figure 5, the resistivity shows a decreasing trend in the range 10^0–10^1 Ω·cm with an increase in Sb sputtering power. The resistivity of thin films mainly depends on the carrier concentration and mobility with the relationship $\rho = 1/nq\mu$, where n, q, and μ represent the carrier concentration, the unit carrier charge, and the carrier mobility, respectively. At the condition of 21 W, a slight increase in resistivity is observed, which is correlated to the lower carrier mobility.

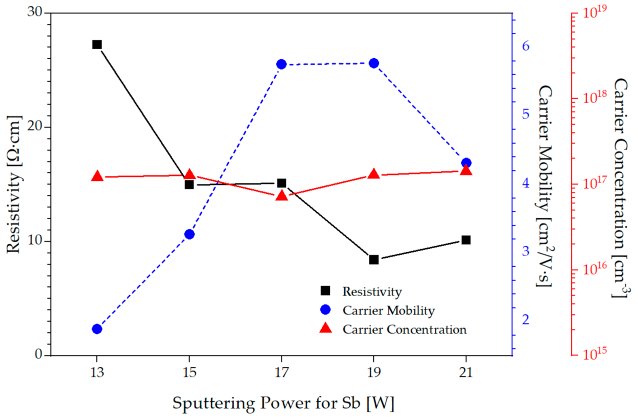

Figure 5. Carrier concentration, resistivity, and carrier mobility in annealed $CuSbSe_2$ thin films as a function of sputtering power for Sb.

Figure 6 illustrates the optical properties of the as-deposited and annealed $CuSbSe_2$ thin films with a change in Sb sputtering power over the spectral region from 200 to 2000 nm. The absorption edge of the as-deposited thin films shifts toward longer wavelengths (red-shift), indicating that the band gap becomes narrower as Sb sputtering power increases, which is due to the Burstein-Moss effect, as shown in Figure 6a. The optical transmittance of the annealed thin films at 13 W shows a similar trend for the as-deposited thin films, as shown in Figure 6a,b; however, the optical transmittance of the annealed thin films converges into much lower values with an increase in Sb sputtering power above 15 W. As shown in Figure 6b, in the visible spectral region 380–780 nm, the mean transmittance of the annealed thin films is 5.19%, 0.64%, 0.52%, 0.24%, and 1.88% for Sb sputtering power of 13, 15, 17, 19, and 21 W, respectively, and increases to 38.26%, 10.15%, 8.85%, 4.77%, and 3.28% for the same powers in the visible and near-infrared (NIR) spectral region 380–1500 nm (inset of Figure 6b), which means that the annealed $CuSbSe_2$ thin films show better optical transmittance as an absorber layer and have similar absorbance capability to the as-deposited thin films in the visible to NIR range. Figure 6c shows the absorbance of the annealed $CuSbSe_2$ thin films. Absorbance is the amount of light absorbed by the sample and can be calculated using the equation $A = -\log T = \log(I_0/I)$, where T is the optical transmittance, I is the intensity of the transmitted radiation, I_0 is the intensity of the incident radiation, and A is the absorbance. The inset of Figure 6c shows the mean values of the absorbance over the 380–780 nm (visible) and the 380–1500 nm (visible to NIR) spectral ranges. In the visible spectral region, the mean absorbance of the annealed thin films is 2.36, 2.84, 3.26, 3.04, and 1.73 for Sb sputtering power of 13, 15, 17, 19, and 21 W, respectively. These values decrease to 1.01, 1.58, 1.63, 1.85, and 1.52 for the same powers in the visible to NIR spectral region. The absorbance of the annealed thin films increases as Sb sputtering power increases, but starts decreasing when gaps appear on the surface. The absorption coefficient (α) was calculated using the Beer–Lambert law in the high-absorption region $\alpha(\upsilon) = (2.303/d)$, where A is the absorbance, υ is the frequency, and d is the thickness of the thin film. Among all of the annealed thin films, the thin film at 15 W shows a stable absorption coefficient of approximately 1.0×10^5 in the range 250–700 nm, which is in accordance with previous reports [6,9,10]. Figure 6d shows the penetration depth (Γ), a parameter measuring how deep an incident photon penetrates below the surface of the thin films before the irradiance decreases to 37% (i.e., $1/e$) of its incident level [50]. All the penetration depths of the annealed thin films were $\leq$194 nm throughout the entire visible spectral range of 380–780 nm, which corresponds to ~10^5 cm^{-1}. In the absorption coefficient plotted on the right axis of Figure 6d, a sharp absorption onset appears just after the band gaps, which is usually observed for direct band gap semiconductors, implying a direct band gap nature for the thin films. The band gaps of the annealed $CuSbSe_2$ thin films were estimated using Tauc's equation $(\alpha h\upsilon)^n = B(h\upsilon - E_g)$, where α is the absorption coefficient, h is Planck's constant (4.135667×10^{-15} eV·s), υ is the photon frequency, B is a constant, and n is the transition probability using 2 for direct allowed transition and $n = 1/2$ for indirect allowed transition. The Tauc plot in Figure 6e illustrates the extrapolation of the straight line part of the curve to $(\alpha h\upsilon)^n = 0$. It was observed that for the films with Sb sputtering powers of 13, 15, 17, and 19 W, the best straight line is obtained for a value of n equal to 2, which is typical of direct allowed transitions [51] and n equal to 1/2 applied for the thin film at 21 W of Sb sputtering power to obtain the best straight line, which indicates indirectly allowed transitions. The extrapolated band gaps of the annealed $CuSbSe_2$ thin films with 13, 15, 17, 19, and 21 W were 1.93, 1.75, 1.74, 1.62, and 3.45 eV, respectively, as shown in Figure 6f. $CuSbSe_2$ has both direct and indirect band gaps, and the reported values are close to each other in the range 1.10–1.05 eV [9,10,52]. The reported band gaps of Cu_2Se are in the range 1.2–2.3 eV [53]. Cu_3SbSe_3 has an indirect band gap with reported band gaps from 0.5 to 1.7 eV, depending on the calculation method [31]. The reported band gaps of Sb_2Se_3 are in the range 1.1–1.8 eV [54]. The band gap values obtained for the thin film with Sb sputtering power of 15–17 W were in the range 1.62–1.93 eV, which is higher than the expected value for $CuSbSe_2$, confirming the presence of other phases in the $CuSbSe_2$ thin films. The band gap value obtained with 21 W was 3.45 eV, which confirms the existence of higher band-gap Sb_2O_3 (3.6–3.9 eV) and sublimation of the lower band-gap phase of Sb_2Se_3 (1.2–1.8 eV) in the $CuSbSe_2$ thin film [15,55].

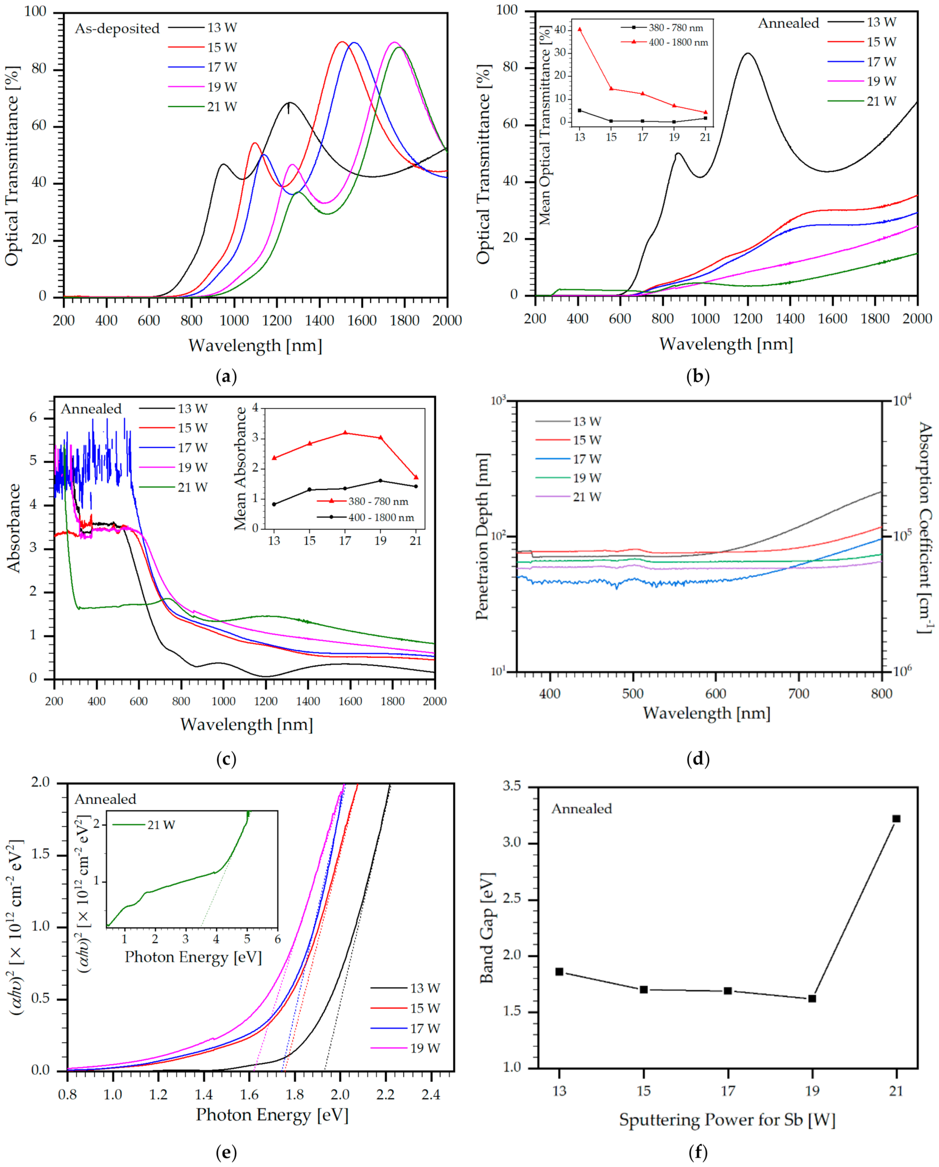

(**a**) (**b**)

(**c**) (**d**)

(**e**) (**f**)

Figure 6. Optical properties of the $CuSbSe_2$ thin films with increasing Sb power: optical transmittance of (**a**) as-deposited and (**b**) annealed thin films. The inset of (**b**) shows the mean optical transmittance in the visible spectral region. (**c**) Absorbance of the annealed thin films and mean absorbance in the visible and near-infrared (NIR) spectral regions as inset. (**d**) Penetration depth and absorption coefficient of annealed thin films in the visible spectral region. (**e**) Tauc plots for determination of the band gap (E_g) of the annealed thin films using linear extrapolation of the leading edge in the direct band gap using $(\alpha h\nu)^2$ for 13–19 W and indirect using $(\alpha h\nu)^{1/2}$ band gap for 21 W as inset. (**f**) Band gap (E_g) of the annealed thin films.

4. Conclusions

Chalcostibite $CuSbSe_2$ thin films were deposited by RF magnetron cosputtering with $CuSe_2$ and Sb targets with varying sputtering power for Sb and RTA treatment for application as the absorber layer in thin-film solar cells. The carrier concentration and resistivity were in the order of 10^{17} cm^{-3} and in the range 10^0–10^1 Ω·cm in the annealed thin films, respectively. The annealed $CuSbSe_2$ thin films showed the good optical properties as an absorber layer in the visible spectral region, such as optical transmittance ≤ 5.19%, penetration depth ≤ 194 nm, absorption coefficient ~10^5 cm^{-1}, and band gaps of 1.62–1.93 eV. Adequate results were also obtained in the NIR spectral region. As the atomic percentage of Sb increased, the probability of forming volatile Sb_2Se_3 (g) increased, leaving large gaps on the surface. Impurity phases in the $CuSbSe_2$ thin films strongly depend on the growth conditions, including the sputtering power for Sb, which determines the optoelectronic properties of $CuSbSe_2$ thin films conclusively. The results of this study reveal the promising optoelectronic characteristics with good morphology and controllable composition in a one-step cosputtering process for $CuSbSe_2$ thin films as an absorber layer for thin-film solar cells in the future, given their Earth abundance and nontoxicity.

Supplementary Materials: The following are available online at http://www.mdpi.com/2079-6412/10/12/1209/s1, Figure S1: Photograph of radio frequency (RF) magnetron cosputtering system (IDT Engineering Co.), Figure S2: Cross-sectional and surface field emission scanning electron microscope (FESEM) images of as-deposited thin films with different sputtering powers for Sb: 13, 15, 17, 19, and 21 W, Table S1: Resistivity (ρ), carrier mobility (μ), and carrier concentration (n) of annealed $CuSbSe_2$ thin films as a function of Sb sputtering power.

Author Contributions: Conceptualization, N.-H.K.; investigation, S.K.; data curation, S.K.; writing—original draft preparation, S.K. and N.-H.K.; writing—review and editing, N.-H.K.; project administration, N.-H.K.; funding acquisition, N.-H.K. All authors have read and agreed to the published version of the manuscript.

Funding: This work was supported by the Korea Institute of Energy Technology Evaluation and Planning (KETEP) and the Ministry of Trade, Industry & Energy (MOTIE) of the Republic of Korea (No. 20184010201650). This study was supported by research fund from Chosun University, 2017.

Conflicts of Interest: The authors declare no conflict of interest. The founding sponsors had no role in the design of the study; in the collection, analyses, or interpretation of data; in the writing of the manuscript, or in the decision to publish the results.

References

1. Nakamura, M.; Yamaguchi, K.; Kimoto, Y.; Yasaki, Y.; Kato, T.; Sugimoto, H. Cd-free $Cu(In,Ga)(Se,S)_2$ thin-film solar cell with record efficiency of 23.35%. *IEEE J. Photovolt.* **2019**, *9*, 1863–1867. [CrossRef]
2. Ravindirana, M.; Praveenkumar, C. Status review and the future prospects of CZTS based solar cell—A novel approach on the device structure and material modeling for CZTS based photovoltaic device. *Renew. Sustain. Energy Rev.* **2018**, *94*, 317–329. [CrossRef]
3. Schorr, S.; Gurieva, G.; Guc, M.; Dimitrievska, M.; Pérez-Rodríguez, A.; Izquierdo-Roca, V.; Schnohr, C.S.; Kim, J.; Jo, W.; Merino, J.M. Point defects, compositional fluctuations, and secondary phases in non-stoichiometric kesterites. *J. Phys. Energy* **2020**, *2*, 012002. [CrossRef]
4. Wang, W.; Winkler, M.T.; Gunawan, O.; Gokmen, T.; Todorov, T.K.; Zhu, Y.; Mitzi, D.B. Device characteristics of CZTSSe thin-film solar cells with 12.6% efficiency. *Adv. Energy Mater.* **2014**, *4*, 1301465. [CrossRef]
5. Yousefi, M.; Minbashi, M.; Monfared, Z.; Memarian, N.; Hajjiah, A. Improving the efficiency of CZTSSe solar cells by engineering the lattice defects in the absorber layer. *Sol. Energy* **2020**, *208*, 884–893. [CrossRef]
6. Peccerillo, E.; Durose, K. Copper–antimony and copper–bismuth chalcogenides—Research opportunities and review for solar photovoltaics. *MRS Energy Sustain.* **2018**, *5*, E13. [CrossRef]
7. Wada, T.; Maeda, T. Optical properties and electronic structures of $CuSbS_2$, $CuSbSe_2$, and $CuSb(S_{1-x}Se_x)_2$ solid solution. *Phys. Status Solidi C* **2017**, *14*, 1600196. [CrossRef]
8. Kumar, M.; Persson, C. $Cu(Sb,Bi)(S,Se)_2$ as Indium-free absorber material with high optical efficiency. *Energy Procedia* **2014**, *44*, 176–183. [CrossRef]
9. Welch, A.W.; Baranowski, L.L.; Zawadzki, P.; Lany, S.; Wolden, C.A.; Zakutayev, A. $CuSbSe_2$ photovoltaic devices with 3% efficiency. *Appl. Phys. Express* **2015**, *8*, 082301. [CrossRef]
10. Xue, D.-J.; Yang, B.; Yuan, Z.-K.; Wang, G.; Liu, X.; Zhou, Y.; Hu, L.; Pan, D.; Chen, S.; Tang, J. $CuSbSe_2$ as a potential photovoltaic absorber material: Studies from theory to experiment. *Adv. Energy Mater.* **2015**, *5*, 1501203. [CrossRef]
11. Li, Z.; Liang, X.; Li, G.; Liu, H.; Zhang, H.; Guo, J.; Chen, J.; Shen, K.; San, X.; Yu, W.; et al. 9.2%-efficient core-shell structured antimony selenide nanorod array solar cells. *Nat. Commun.* **2019**, *10*, 125. [CrossRef] [PubMed]
12. Skoug, E.J.; Morelli, D.T. Role of lone-pair electrons in producing minimum thermal conductivity in nitrogen-group chalcogenide compounds. *Phys. Rev. Lett.* **2011**, *107*, 235901. [CrossRef] [PubMed]

13. Eraky, M.S.; Sanad, M.M.S.; El-Sayed, E.M.; Shenouda, A.Y.; El-Sherefy, E.-S. Phase transformation and photoelectrochemical characterization of Cu/Bi and Cu/Sb based selenide alloys as promising photoactive electrodes. *AIP Adv.* **2019**, *9*, 115115. [CrossRef]
14. Wang, C.; Yang, B.; Ding, R.; Chen, W.; Kondrotas, R.; Zhao, Y.; Lu, S.; Li, Z.; Tang, J. Reactive close-spaced sublimation processed $CuSbSe_2$ thin films and their photovoltaic application. *APL Mater.* **2018**, *6*, 084801. [CrossRef]
15. Tiwari, K.J.; Vinod, V.; Subrahmanyam, A.; Malar, P. Growth and characterization of chalcostibite $CuSbSe_2$ thin films for photovoltaic application. *Appl. Surf. Sci.* **2017**, *418*, 216–224. [CrossRef]
16. Zhang, D.; Yang, J.; Jiang, Q.; Fu, L.; Xiao, Y.; Luo, Y.; Zhou, Z. Ternary $CuSbSe_2$ chalcostibite: Facile synthesis, electronic-structure and thermoelectric performance enhancement. *J. Mater. Chem. A* **2016**, *4*, 4188–4193. [CrossRef]
17. Ismailova, E.N.; Mashadieva, L.F.; Bakhtiyarly, I.B.; Babanly, M.B. Phase equilibria in the Cu_2Se-SnSe-$CuSbSe_2$ system. *Russ. J. Inorg. Chem.* **2019**, *64*, 801–809. [CrossRef]
18. Yang, B.; Wang, C.; Yuan, Z.; Chen, S.; He, Y.; Song, H.; Ding, R.; Zhao, Y.; Tang, J. Hydrazine solution processed $CuSbSe_2$: Temperature dependent phase and crystal orientation evolution. *Sol. Energy Mater. Sol. Cells* **2017**, *168*, 112–118. [CrossRef]
19. Yan, H.; Xiao, R.; Pei, Y.; Yang, K.; Li, B. Structural, electrical and optical characteristics of $CuSbSe_2$ films prepared by pulsed laser deposition and magnetron sputtering processes. *J. Mater. Sci. Mater. Electron.* **2020**, *31*, 644–651. [CrossRef]
20. Oh, S.; Park, Y.S.; Ko, P.J.; Kim, N.-H. Effects of rapid thermal treatment on properties of magnetron-sputtered NiO thin films for supercapacitor applications. *J. Nanosci. Nanotechnol.* **2018**, *18*, 6213–6219. [CrossRef]
21. Welch, A.W.; Baranowski, L.L.; Peng, H.; Hempel, H.; Eichberger, R.; Unold, T.; Lany, S.; Wolden, C.; Zakutayev, A. Trade-offs in thin film solar cells with layered chalcostibite photovoltaic absorbers. *Adv. Energy Mater.* **2017**, *7*, 1601935. [CrossRef]
22. Cang, Q.; Guo, H.; Jia, X.; Ning, H.; Ma, C.; Zhang, J.; Yuan, N.; Ding, J. Enhancement in the efficiency of Sb_2Se_3 solar cells by adding low lattice mismatch $CuSbSe_2$ hole transport layer. *Sol. Energy* **2020**, *199*, 19–25. [CrossRef]
23. Gilić, M.; Petrović, M.; Kostić, R.; Stojanović, D.; Barudžija, T.; Mitrić, M.; Romčević, N.; Ralević, U.; Trajić, J.; Romčević, M.; et al. Structural and optical properties of $CuSe_2$ nanocrystals formed in thin solid Cu–Se film. *Infrared Phys. Technol.* **2016**, *76*, 276–284. [CrossRef]
24. Yoo, M.H.; Ko, P.J.; Kim, N.-H.; Lee, H.-Y. Cu(In,Ga)Se_2 thin films annealed using a continuous wave Nd:YAG laser (λ_o = 532 nm): Effects of laser-annealing time. *J. Korean Phys. Soc.* **2017**, *71*, 1038–1047. [CrossRef]
25. Moon, E.-A.; Jun, Y.-K.; Kim, N.-H.; Lee, W.-S. Heavily-doped ZnO:Al thin films prepared by using magnetron co-sputtering: Optical and electrical properties. *J. Korean Phys. Soc.* **2016**, *69*, 220–225. [CrossRef]
26. Sun, X.H.; Pan, Y.P.; Dong, L.; Zhao, M.L.; Wan, R.X.; Gu, H.Q.; Li, D.J. Modulation period of Ag deposition on co-sputtered TiN-Ag leading to different microstructures: Implication on mechanical properties and living cells growth. *Surf. Coat. Technol.* **2017**, *326*, 382–387. [CrossRef]
27. Joung, Y.-H.; Kang, H.I.; Kim, J.H.; Lee, H.-S.; Lee, J.; Choi, W.S. SiC formation for a solar cell passivation layer using an RF magnetron co-sputtering system. *Nanoscale Res. Lett.* **2012**, *7*, 22. [CrossRef]
28. Wen, X.; Chen, C.; Lu, S.; Li, K.; Kondrotas, R.; Zhao, Y.; Chen, W.; Gao, L.; Wang, C.; Zhang, J.; et al. Vapor transport deposition of antimony selenide thin film solar cells with 7.6% efficiency. *Nat. Commun.* **2018**, *9*, 2179. [CrossRef]
29. Dabaa, B.; Srouji, F.; Brgol, M. Electrical, structural and optical properties of Cu_3SbSe_4 with high thermoelectric performance. *Nano Sci. Nano Technol. Indian J.* **2018**, *12*, 124. Available online: https://www.tsijournals.com/articles/electrical-structural-and-optical-properties-of-cu3sbse4-with-high-thermoelectric-performance-13738.html (accessed on 1 November 2020).
30. Tyagi, K.; Gahtori, B.; Bathula, S.; Srivastava, A.K.; Shukla, A.K.; Auluck, S.; Dhar, A. Thermoelectric properties of Cu_3SbSe_3 with intrinsically ultralow lattice thermal conductivity. *J. Mater. Chem. A* **2014**, *2*, 15829–15835. [CrossRef]
31. Wei, T.-R.; Wu, C.-F.; Sun, W.; Pan, Y.; Li, J.-F. Is Cu_3SbSe_3 a promising thermoelectric material? *RSC Adv.* **2015**, *5*, 42848–42854. [CrossRef]
32. Ko, T.-Y.; Shellaiah, M.; Sun, K.W. Thermal and thermoelectric transport in highly resistive single Sb_2Se_3 nanowires and nanowire bundles. *Sci. Rep.* **2016**, *6*, 35086. [CrossRef]

33. Chen, S.; Qiao, X.; Zheng, Z.; Cathelinaud, M.; Ma, H.; Fan, X.; Zhang, X. Enhanced electrical conductivity and photoconductive properties of Sn-doped Sb_2Se_3 crystals. *J. Mater. Chem. C* **2018**, *6*, 6465–6470. [CrossRef]
34. Liu, Y.-Q.; Zhang, M.; Wang, F.-X.; Pan, G.-B. Facile microwave-assisted synthesis of uniform Sb_2Se_3 nanowires for high performance photodetectors. *J. Mater. Chem. A* **2014**, *2*, 240–244.
35. Pattini, F.; Rampino, S.; Mezzadri, F.; Calestani, D.; Spaggiari, G.; Sidoli, M.; Delmonte, D.; Sala, A.; Gilioli, E.; Mazzer, M. Role of the substrates in the ribbon orientation of Sb_2Se_3 films grown by low-temperature pulsed electron deposition. *Sol. Energy Mater. Sol. Cells* **2020**, *218*, 110724. [CrossRef]
36. Ghosh, S.; Moreira, M.V.B.; Fantini, C.; Gonzalez, J.C. Growth and optical properties of nanocrystalline Sb_2Se_3 thin-films for the application in solar-cells. *Sol. Energy* **2020**, *211*, 613–621. [CrossRef]
37. Hamrouni, R.; Segmane, N.E.H.; Abdelkader, D.; Amara, A.; Drici, A.; Bououdina, M.; Akkari, F.C.; Khemiri, N.; Bechiri, L.; Kanzari, M.; et al. Linear and non linear optical properties of Sb_2Se_3 thin films elaborated from nano-crystalline mechanically alloyed powder. *Appl. Phys. A* **2018**, *124*, 861. [CrossRef]
38. Hsiang, H.-I.; Yang, C.-T.; Tu, J.-H. Characterization of $CuSbSe_2$ crystallites synthesized using a hot injection method. *RSC Adv.* **2016**, *6*, 99297–99305. [CrossRef]
39. Riha, S.C.; Johnson, D.C.; Prieto, A.L. Cu_2Se nanoparticles with tunable electronic properties due to a controlled solid-state phase transition driven by copper oxidation and cationic conduction. *J. Am. Chem. Soc.* **2011**, *133*, 1383–1390. [CrossRef]
40. Liu, Y.; Yang, J.; Gu, E.; Cao, T.; Su, Z.; Jiang, L.; Yan, C.; Hao, X.; Liu, F.; Liu, Y. Colloidal synthesis and characterisation of Cu_3SbSe_3 nanocrystals. *J. Mater. Chem. A* **2014**, *2*, 6363–6367. [CrossRef]
41. Biesinger, M.C. Advanced analysis of copper X-ray photoelectron spectra. *Surf. Interface Anal.* **2017**, *49*, 1325–1334. [CrossRef]
42. Nyholm, R.; Martensson, N.; Lebugle, A.; Axelsson, U. Auger and Coster-Kronig broadening effects in the 2*p* and 3*p* photoelectron spectra from the metals ^{22}Ti-^{30}Zn. *J. Phys. F Met. Phys.* **1981**, *11*, 1727–1733. [CrossRef]
43. Qiao, J.; Zhao, Y.; Jin, Q.; Tan, J.; Kang, S.; Qiu, J.; Tai, K. Tailoring nanoporous structures in Bi_2Te_3 thin films for improved thermoelectric performance. *ACS Appl. Mater. Interfaces* **2019**, *11*, 38075–38083. [CrossRef]
44. Krishnan, B.; Shaji, S.; Ornelas, R.E. Progress in development of copper antimony sulfide thin films as an alternative material for solar energy harvesting. *J. Mater. Sci. Mater. Electron.* **2015**, *26*, 4770–4781. [CrossRef]
45. Chen, C.; Bobela, D.C.; Yang, Y.; Lu, S.; Zeng, K.; Ge, C.; Yang, B.; Gao, L.; Zhao, Y.; Beard, M.C.; et al. Characterization of basic physical properties of Sb_2Se_3 and its relevance for photovoltaics. *Front. Optoelectron.* **2017**, *10*, 18–30. [CrossRef]
46. Shinde, U.P. Hall coefficient, mobility and carrier concentration as a function of composition and thickness of Zn-Te thin films. *Adv. Appl. Sci. Res.* **2015**, *4*, 215–220.
47. Li, Z.-Q.; Ni, M.; Feng, X.-D. Simulation of the Sb_2Se_3 solar cell with a hole transport layer. *Mater. Res. Express* **2020**, *7*, 016416. [CrossRef]
48. Firdausa, C.M.; Rizam, M.S.B.S.; Rusop, M.; Hidayah, S.R. Characterization of ZnO and ZnO: TiO_2 thin films prepared by sol-gel spray-spin coating technique. *Procedia Eng.* **2012**, *41*, 1367–1373. [CrossRef]
49. Aduda, B.O.; Ravirajan, P.; Choy, K.L.; Nelson, J. Effect of morphology on electron drift mobility in porous TiO_2. *Int. J. Photoenergy* **2004**, *6*, 141–147. [CrossRef]
50. Park, C.I.; Kim, N.-H. Hydrogenation in 808-nm diode laser annealing of CdTe thin films: Structural, optical, and electrical properties. *Sci. Adv. Mater.* **2016**, *8*, 1813–1818. [CrossRef]
51. Tauc, J. Optical properties and electronic structure of amorphous Ge and Si. *Mater. Res. Bull.* **1968**, *3*, 37–46. [CrossRef]
52. Rampino, S.; Pattini, F.; Bronzoni, M.; Mazzer, M.; Sidoli, M.; Spaggiari, G.; Gilioli, E. $CuSbSe_2$ thin film solar cells with ~4% conversion efficiency grown by low-temperature pulsed electron deposition. *Sol. Energy Mater. Sol. Cells* **2018**, *185*, 86–96. [CrossRef]
53. Sudha, A.P.; Henry, J.; Mohanraj, K.; Sivakumar, G. Synthesis and characterization of monovalent, divalent and trivalent cation doping of Cu_2Se thin films using chemical bath deposition method. *Jordan J. Phys.* **2018**, *11*, 125–130.
54. Rath, T.; MacLachlan, A.J.; Brown, M.D.; Haque, S.A. Structural, optical and charge generation properties of chalcostibite and tetrahedrite copper antimony sulfide thin films prepared from metal xanthates. *J. Mater. Chem. A* **2015**, *3*, 24155–24162. [CrossRef] [PubMed]

55. Lakhdar, M.H.; Smida, Y.B.; Amlouk, M. Synthesis, optical characterization and DFT calculations of electronic structure of Sb_2O_3 films obtained by thermal oxidation of Sb_2S_3. *J. Alloys Compd.* **2016**, *681*, 197–204. [CrossRef]